Modulation of the Global Atmospheric Circulation by Combined Activity in the Madden–Julian Oscillation and the El Niño–Southern Oscillation during Boreal Winter

PAUL E. ROUNDY, KYLE MACRITCHIE, JONAS ASUMA, AND TIMOTHY MELINO

University at Albany, State University of New York, Albany, New York

ABSTRACT

Composite global patterns associated with the El Niño–Southern Oscillation (ENSO) and the Madden–Julian oscillation (MJO) are frequently applied to help make predictions of weather around the globe at lead times beyond a few days. However, ENSO modulates the background states through which the MJO and its global response patterns propagate. This paper explores the possibility that nonlinear variations confound the combined use of composites based on the MJO and ENSO separately. Results indicate that when both modes are active at the same time, the associated patterns in the global flow are poorly represented by simple linear combinations of composites based on the MJO and ENSO individually. Composites calculated by averaging data over periods when both modes are present at the same time more effectively describe the associated weather patterns. Results reveal that the high-latitude response to the MJO varies with ENSO over all longitudes, but especially across the North Pacific Rim, North America, and the North Atlantic. Further analysis demonstrates that the MJO influence on indexes of the North Atlantic Oscillation is greatest during La Niña conditions or during periods of rapid adjustment in the phase of ENSO.

1. Introduction

Prediction of midlatitude weather at lead times longer than four or five days depends on the geographical distribution and temporal evolution of moist deep convection in the tropics (Wallace and Gutzler 1981; Ferranti et al. 1990; Weickmann et al. 1997; Mo and Higgins 1998; Hendon et al. 2000; Higgins et al. 2000; Jones and Schemm 2000; Nogues-Paegle et al. 2000; Mo 2000; Branstator 2002; Jones et al. 2004a,b; Weickmann and Berry 2007). This dependence is a consequence of redistribution of mass by the convection, which is associated with broad-scale overturning circulations, global and regional cycles of atmospheric angular momentum (Weickmann and Sardeshmukh 1994; Weickmann and Berry 2009), and Rossby wave trains that extend eastward and poleward across the midlatitudes (Sardeshmukh and Hoskins 1988; Jin and Hoskins 1995; Bladé and Hartmann 1995). These patterns profoundly influence extratropical storm tracks around the world.

Such seasonal teleconnection patterns have long been associated with the El Niño–Southern Oscillation (ENSO; Charney and Shukla 1981; Brankovic et al. 1994) and the Madden–Julian oscillation (MJO; e.g., Matthews et al. 2004; Zhang 2005). The MJO is a planetary-scale, eastward-propagating pattern of winds and moist deep convection characterized by 30–60-day periods that have no broadly accepted dynamical explanation. Many authors have utilized patterns associated with the MJO and ENSO individually to predict variations of the global flow. Those who apply these results might consider using their linear combinations when both modes occur simultaneously. However, ENSO modifies the background state of moist deep convection, wind, and temperature through which the MJO and its associated global patterns propagate. Pohl and Matthews (2007) demonstrated that ENSO modulates the propagation characteristics of the MJO itself; however, the different background states might also lead to different global circulation patterns associated with the MJO during different phases of ENSO. Should the response patterns to the MJO change substantially with different phases of ENSO, linear approaches would not sufficiently diagnose the global patterns associated with the two modes acting in concert. The purpose of this work is to determine the global circulation patterns associated with the MJO during

Corresponding author address: Paul E. Roundy, Department of Atmospheric and Environmental Sciences, University at Albany, DAES-ES351, Albany, NY 12222.
E-mail: roundy@atmos.albany.edu

70–Days of MJO EEOF PCs, ending 12–Mar–2005
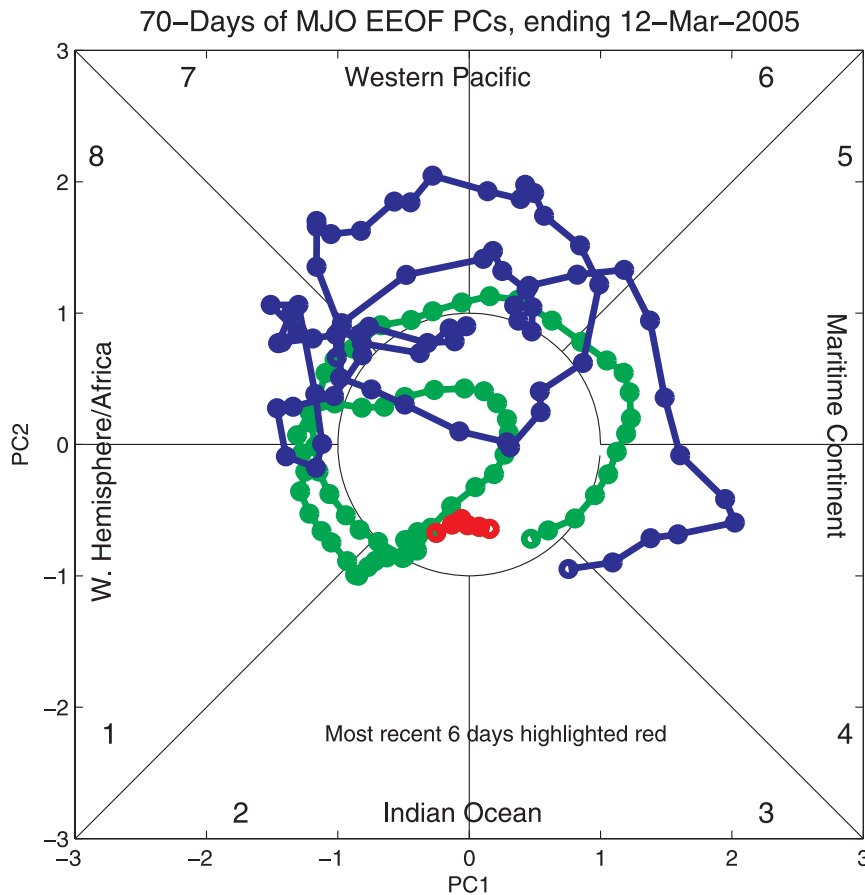
FIG. 1. Phase diagram for the modified RMM PCs for early 2005 (green curve, ending in red). Standard RMM PCs following Wheeler and Hendon (2004) are plotted for the same period for reference (blue curve).

the warm and cold and warming and cooling phases of ENSO during extended boreal winter and to diagnose the significance and magnitude of patterns associated with nonlinear interaction between ENSO, the MJO, and the global flow. We emphasize mid- and higher-latitude patterns. Section 2 describes the data applied, section 3 describes a composite analysis to determine the significance and scope of the nonlinear components of the flow, and section 4 summarizes our results.

2. Data

Interpolated outgoing longwave radiation (OLR; Liebmann and Smith 1996) and Centers for Environmental Prediction–National Center for Atmospheric Research (NCEP–NCAR) reanalysis (Kalnay et al. 1996) 300-hPa geopotential height data were obtained from the Earth System Research Laboratory (ESRL). Anomalies were generated by subtracting the local mean and the seasonal cycle (along with its first three harmonics) estimated for the period 1974–2008. An analysis of streamfunction on the 0.2 sigma-level surface is similar across

the global extratropics, but we apply geopotential height to emphasize the high-latitude features that are the focus of this work. Monthly Niño-3.4 SST anomalies were obtained from the National Oceanic and Atmospheric Administration (NOAA)'s Climate Prediction Center (CPC). To more fully diagnose the broader influence of ENSO, we also include analysis based on an index of the temporal trend of ENSO, generated by taking the first time finite difference of the Niño-3.4 SST anomalies across each individual month. A daily index of the North Atlantic Oscillation (NAO) was obtained from the CPC.

A modification of the Wheeler and Hendon (2004) real-time multivariate MJO (RMM) indexes is applied to track the phase of the MJO. These indexes allow for easy calculation of composites based on eight broadly recognized geographical phases of the MJO. However, indexes generated following Wheeler and Hendon (2004) vary erratically from day to day, because they include signals associated with convectively coupled equatorial waves—especially the Kelvin wave (Roundy et al. 2009) and other signals not explained by the MJO. To enhance
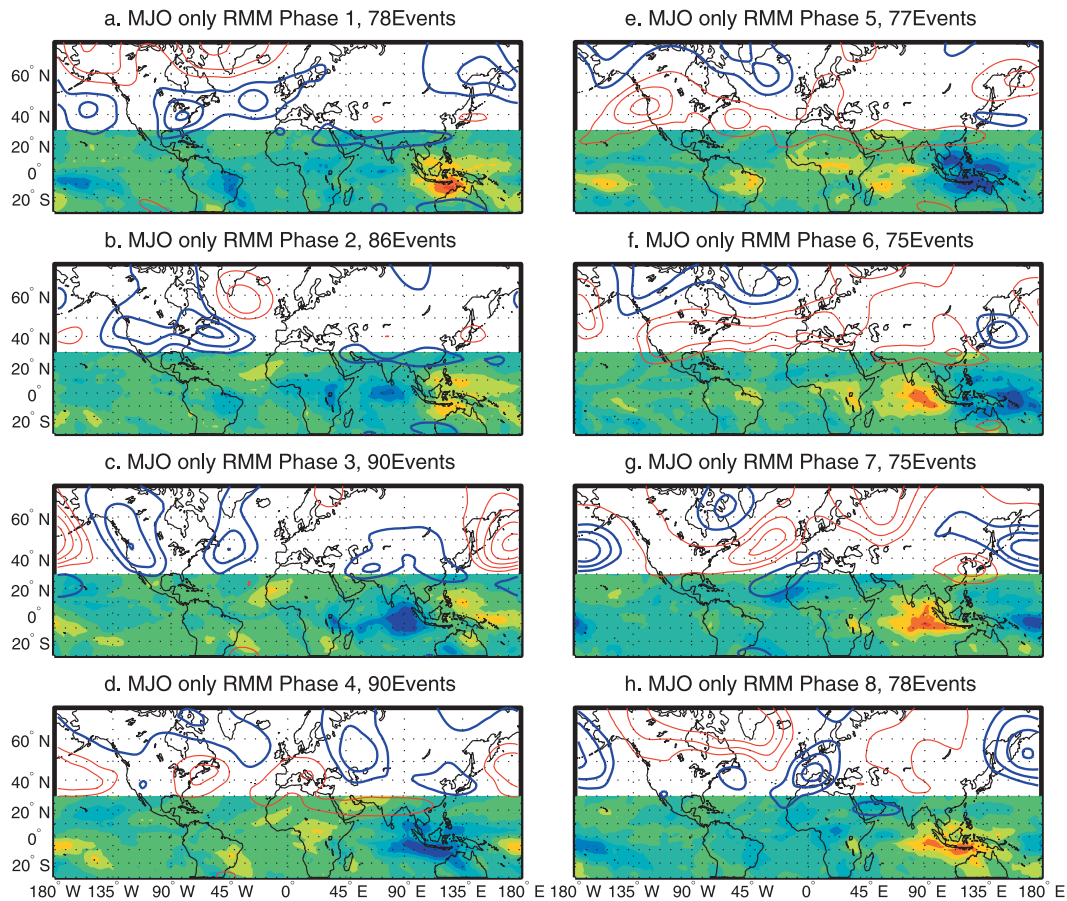
FIG. 2. Composite 300-hPa geopotential height (contours, blue indicates negative and red indicates positive) and OLR anomalies (shading, blue suggests active convection). The panels represent phases 1–8 of the MJO (based on the modified RMM PCs described in section 2). The contour interval is 15 m, and the zero contour is omitted.

the focus on the MJO itself, the spatial patterns of the first two empirical orthogonal functions (EOFs) associated with the RMM indexes were obtained from the Australian Bureau of Meteorology Web site. A pair of the corresponding principal components (PCs) for the MJO was then constructed by projecting OLR and wind data prefiltered for the MJO band of the wavenumber frequency domain and averaged over 15°N–15°S onto these EOFs. Our filter band includes wavenumbers 0–10 eastward and periods of 30–100 days. Similar filter bands have been applied by others, such as Wheeler and Kiladis (1999; wavenumbers 1–5), Roundy and Frank (2004; wavenumbers 0–6), and Roundy (2008; wavenumbers 0–10). This filtering was applied by following the time-extended EOF (EEOF) projection technique of Roundy and Schreck (2009). All six steps in the Roundy and Schreck projection process were applied. The filtered data are the projections of unfiltered OLR anomalies onto the first 40 EEOFs of the MJO band, taking the 0-day time lag. Roundy and Schreck showed that the

results are similar to those based on direct filtering in the wavenumber–frequency domain by Fourier methods. The principal advantage of the projection approach over direct filtering is that the patterns analyzed here can also be applied in real time, because the projection algorithm does not distinguish between results at the end or the interior of the dataset.

The filtering removes most signals associated with other modes from the PCs along with other noise. It also provides a more complete exclusion of ENSO signals from the PCs than can be obtained by following Wheeler and Hendon (2004), because their approach would retain some ENSO signal during periods of rapid ENSO adjustment. The resulting PC1 and PC2 are shown plotted in green and red on Fig. 1 for a randomly selected period (during early 2005). The corresponding Wheeler and Hendon (2004) RMM PCs are plotted in blue for comparison. The modified PCs revolve more smoothly about the origin, whereas for this case the center of revolution of the RMM PCs evolves upward with time. The spectrum

a. OLR&300 Ht.,NM, Nino 3.4 Declining

b. OLR&300 Ht.,NM, Nino 3.4 Negative

c. OLR&300 Ht.,NM, Nino 3.4 Rising

d. OLR&300 Ht.,NM, Nino 3.4 Positive
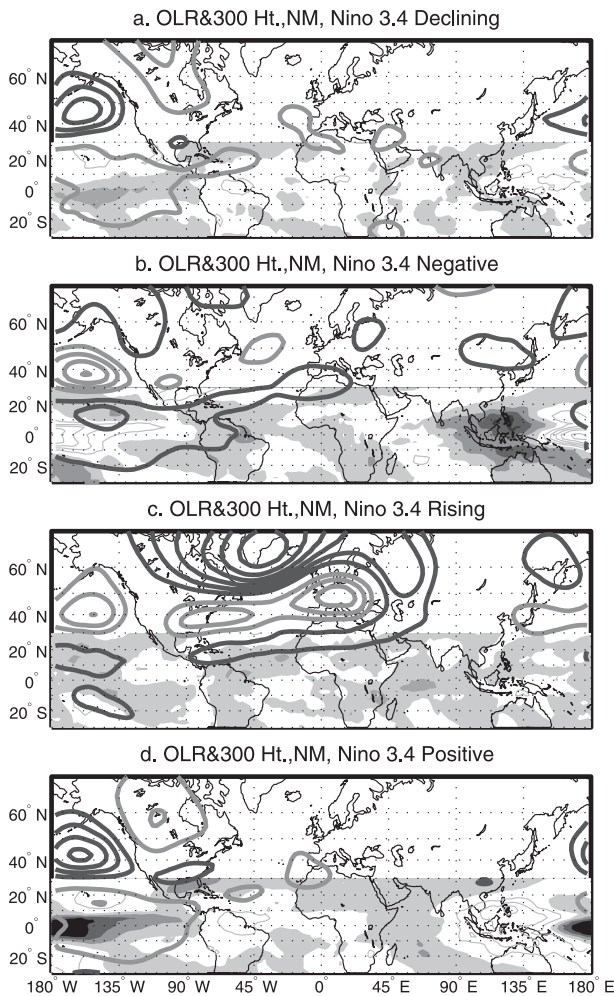
FIG. 3. Composite 300-hPa geopotential height (contours, dark gray indicates negative and light gray indicates positive) and OLR anomalies (negative anomalies are shaded, suggesting active convection) for (a) negative temporal trend in Niño-3.4 SST, (b) negative Niño-3.4 SST, (c) increasing Niño-3.4 SST, and (d) Niño-3.4 positive. The contour interval is 15 m, and the zero contour is omitted.

of the MJO projections is much more confined in the region of the MJO peak in the wavenumber–frequency domain (Roundy and Schreck 2009) than in the spectrum of the RMM PCs (see Wheeler and Hendon 2004), suggesting that the resulting signal is more pure than the unprocessed RMM signals. The correlation coefficient of the modified PC1 to RMM PC1 is 0.65 (for all available data 1975–2006). Further, composites generated from the modified PCs exhibit higher anomaly amplitudes than those generated from the RMM PCs, even though roughly the same number of MJO events are included (not shown), suggesting that the reduction of the noise produces more robust results. We generate from the modified PCs a time series of MJO phase, following the geographical

breakdown of Wheeler and Hendon (2004), as noted in Fig. 1.

3. Compositing approach

Composites were calculated by averaging fields of data over lists of dates obtained from the analysis of the MJO and ENSO indexes. Only events during November–March (NM) were included. Note that results are sensitive to the seasons analyzed, such that in general, one cannot expect results obtained during one season to apply during another season. Three sets of composites were made. The first set of composites was based on averaging data over all dates when the modified RMM PCs indicated that the amplitude of the MJO in a given phase exceeded ±1 standard deviation (SD) in the daily indices. The second set of composites was generated by averaging data over the set of all dates when the selected ENSO index (Niño-3.4 or Niño-3.4 temporal trend) was positive or negative and greater than 0.75 SDs. The composites based on ENSO alone do not contain any explicit information about the MJO. These MJO- and ENSO-based composites are labeled "individual" composites for simplicity, since they depend explicitly on only one mode. The third set of composites was then calculated for each phase of the MJO that occurred during the selected ENSO phase. These "simultaneous" composites would include the effects of nonlinear modulation of the MJO and its associated global patterns by ENSO.

The individual and simultaneous composites were then combined and compared systematically to isolate any nonlinear signal. We first subtracted the composite based on a given phase of ENSO from the corresponding simultaneous composite. We then subtracted the individual composite for the MJO. The resulting residual estimates the nonlinear contribution to simultaneous activity by the MJO and ENSO. We assessed the statistical significance by a 1000-iteration bootstrap resampling test, following the approaches of Roundy (2008), Roundy and Kravitz (2009), and Wilks (2006). These tests were complicated by different numbers of degrees of freedom associated with different numbers of MJO events included in the different composites. The individual and simultaneous composites need to be compared in similar contexts, but composites containing fewer MJO events would most likely include higher-amplitude anomalies. The simultaneous composites include roughly one-third the number of MJO events as the individual composites for the MJO.

To test the sensitivity of the results to the number of events in the composites, new composites for each MJO phase were generated by averaging over many random selections of the original events (selected with replacement), limiting the number of MJO events included in each

a. Nino 3.4 neg., Combined RMM Phase 1, 21 Events   e. Nino 3.4 neg., Combined RMM Phase 5, 16 Events

b. Nino 3.4 neg., Combined RMM Phase 2, 16 Events   f. Nino 3.4 neg., Combined RMM Phase 6, 19 Events

c. Nino 3.4 neg., Combined RMM Phase 3, 20 Events   g. Nino 3.4 neg., Combined RMM Phase 7, 19 Events

d. Nino 3.4 neg., Combined RMM Phase 4, 22 Events   h. Nino 3.4 neg., Combined RMM Phase 8, 22 Events
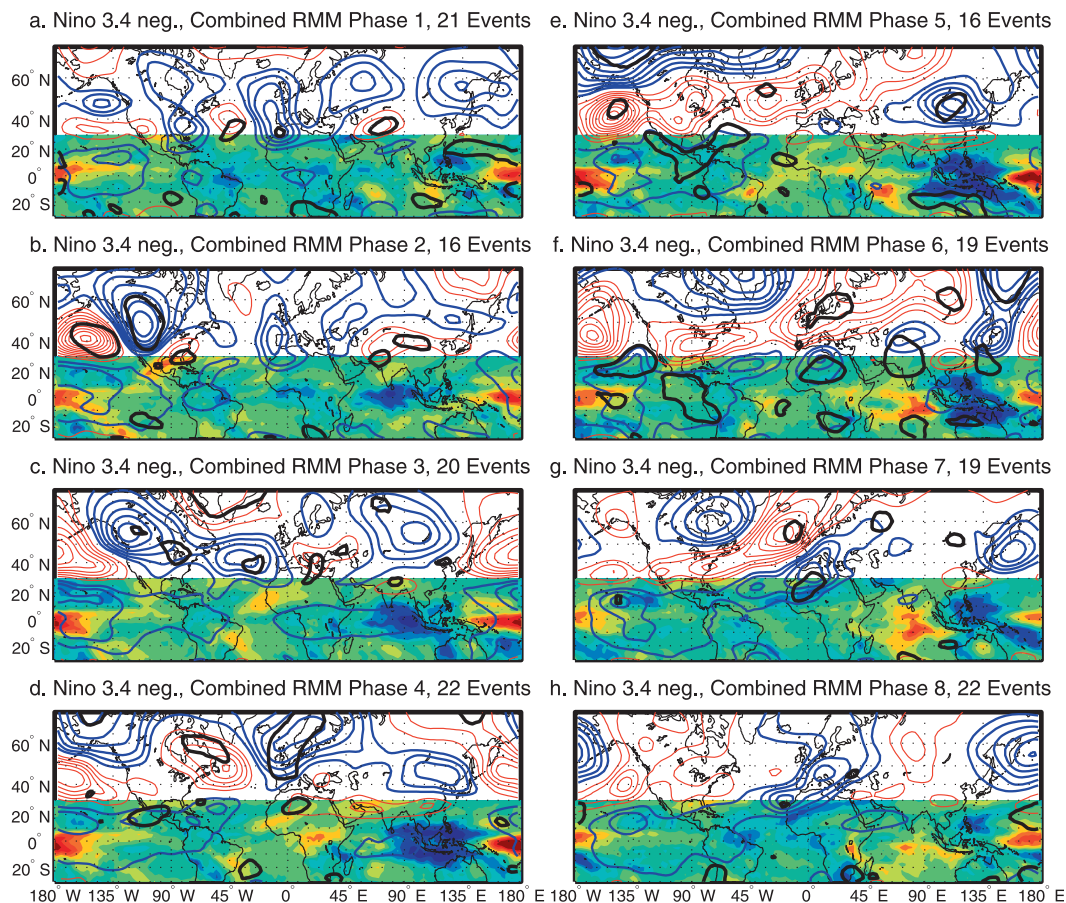
FIG. 4. Composite patterns based on simultaneous occurrence of cold ENSO conditions and the MJO, with (a)–(h) showing MJO phases 1–8, plotted as in Figs. 2–3. Thick black curves enclose the 90% level for difference from zero of the nonlinear component of the composite pattern, as discussed in section 2.

average to be the same as in the simultaneous composites. An MJO event was considered a string of consecutive days when the MJO was found to be in a particular phase. The resulting distribution of means is broader than that obtained by following the standard bootstrap test for the difference of two means (e.g., Wilks 2006), making the significance tests more restrictive. The relevant number of degrees of freedom is the number of distinct MJO events in the simultaneous composite. Final results provide relative amplitude scales (along with the corresponding confidence intervals) for the contribution of nonlinear interactions between the global patterns associated with the MJO and ENSO.

4. Results

a. Composite global patterns associated with the MJO

We first review composite patterns for ENSO and the MJO individually and then we discuss the simultaneous

composites. Figures 2a–h show composites based on the MJO phases 1–8 respectively, for NM, without respect to ENSO. Results are broadly consistent with the observational analysis of Matthews et al. (2004). Geopotential height anomalies associated with each MJO phase are distributed globally, but they attain their highest amplitudes around the North Pacific Rim eastward to the North Atlantic. The highest amplitude anomalies exceed 70 m.

b. Composite global patterns associated with ENSO

Figures 3a–d shows composite OLR and geopotential height for negative ENSO trend (<0.75 SD in the first time finite difference in Niño-3.4 SST), cold ENSO (<−0.75 SD Niño-3.4 SST), warming ENSO, and warm ENSO, respectively. The negative ENSO trend (Fig. 3a) is associated with a pronounced trough anomaly over the north-central Pacific and a ridge anomaly over north-central Canada. The La Niña signature (Fig. 3b) consists largely of enhanced convection over the Maritime

a. Nino 3.4 neg., Nonlinear, RMM Phase 1, 21 Events   e. Nino 3.4 neg., Nonlinear, RMM Phase 5, 16 Events

b. Nino 3.4 neg., Nonlinear, RMM Phase 2, 16 Events   f. Nino 3.4 neg., Nonlinear, RMM Phase 6, 19 Events

c. Nino 3.4 neg., Nonlinear, RMM Phase 3, 20 Events   g. Nino 3.4 neg., Nonlinear, RMM Phase 7, 19 Events

d. Nino 3.4 neg., Nonlinear, RMM Phase 4, 22 Events   h. Nino 3.4 neg., Nonlinear, RMM Phase 8, 22 Events
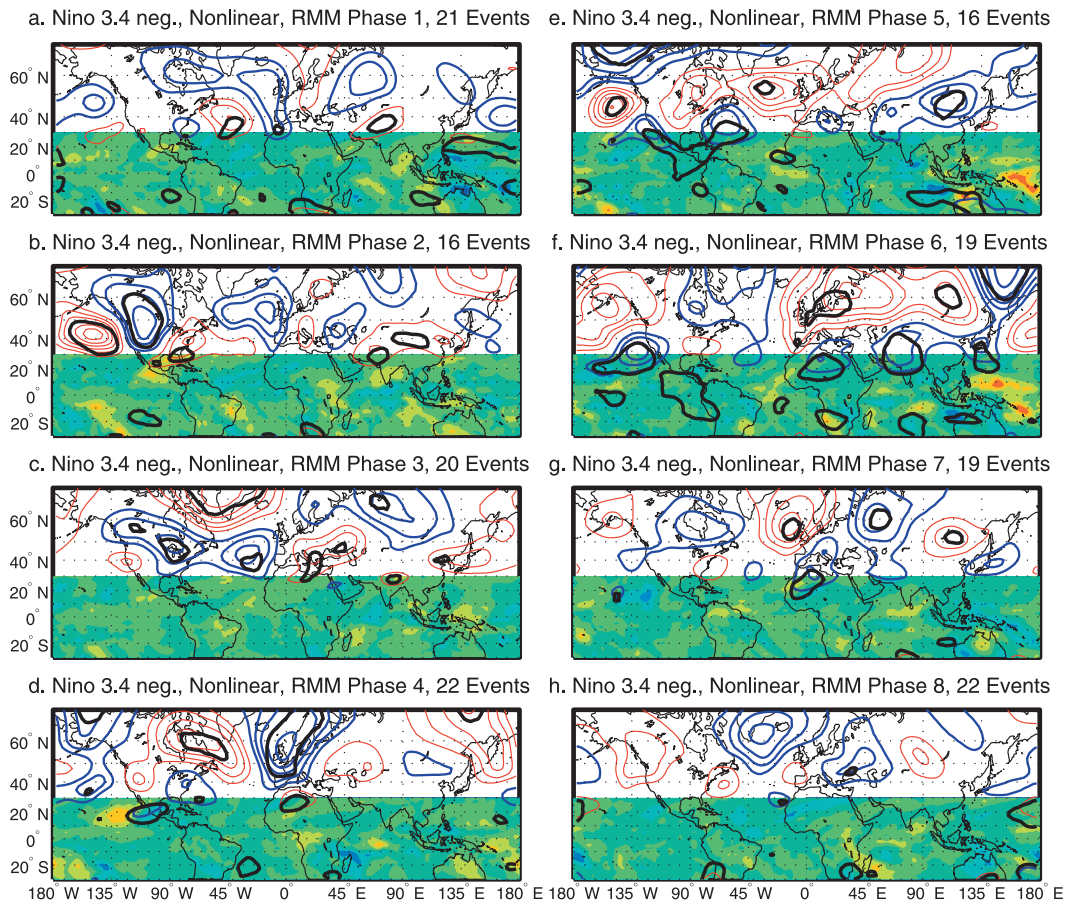
FIG. 5. Composites based on simultaneous cold ENSO conditions and the MJO, minus the composite based on cold ENSO (Fig. 4) and the corresponding composite patterns based on the MJO alone (Fig. 2), with (a)–(h) showing MJO phases 1–8.

Continent, with suppressed convection across the central equatorial Pacific. Trough anomalies occur just off the equator over the east Pacific, with a broad ridge anomaly over the temperate latitudes of the northeast Pacific. Warming ENSO (Fig. 3c) is associated with a ridge over the north-central Pacific and another ridge over the Atlantic region extending from the eastern United States eastward across western Europe. Substantial trough anomalies occur near Greenland and northwestern Russia. Anomalies during El Niño (Fig. 3d) are generally opposite those of La Niña, with the most prominent exception a more pronounced ridge anomaly over western Canada.

c. Simultaneous composites: Cold ENSO and the MJO

Figure 4 shows the simultaneous composite for each MJO phase during cold ENSO. Thick black contours enclose regions in which anomalies are characterized by significantly different patterns from those obtained by

a sum of the corresponding individual MJO and ENSO composites (Figs. 2b and 3).

The pattern of global geopotential height during phase 1 and cold ENSO is similar to that for the MJO only. Significant differences occur in isolated small regions, including the northern subtropical Atlantic and a portion of southwest Asia.

During phase 2 and cold ENSO, a pronounced trough occurs over western North America with a ridge over the north-central Pacific. The ridge that is apparent over the North Atlantic in Fig. 2b is largely absent.

The general pattern during MJO phase 3 and La Niña is similar to that during phase 3 in the individual composite but with higher amplitudes across the globe. Principal exceptions to this observation are that the trough anomalies over western North America and the north-central Atlantic apparently unite under a single closed contour during La Niña. Southern Europe experiences significant ridge anomalies, and a ridge anomaly appears over Greenland.

a. Nino 3.4 decl., Nonlinear, RMM Phase 1, 14 Events   e. Nino 3.4 decl., Nonlinear, RMM Phase 5, 16 Events

b. Nino 3.4 decl., Nonlinear, RMM Phase 2, 18 Events   f. Nino 3.4 decl., Nonlinear, RMM Phase 6, 19 Events

c. Nino 3.4 decl., Nonlinear, RMM Phase 3, 17 Events   g. Nino 3.4 decl., Nonlinear, RMM Phase 7, 16 Events

d. Nino 3.4 decl., Nonlinear, RMM Phase 4, 17 Events   h. Nino 3.4 decl., Nonlinear, RMM Phase 8, 14 Events
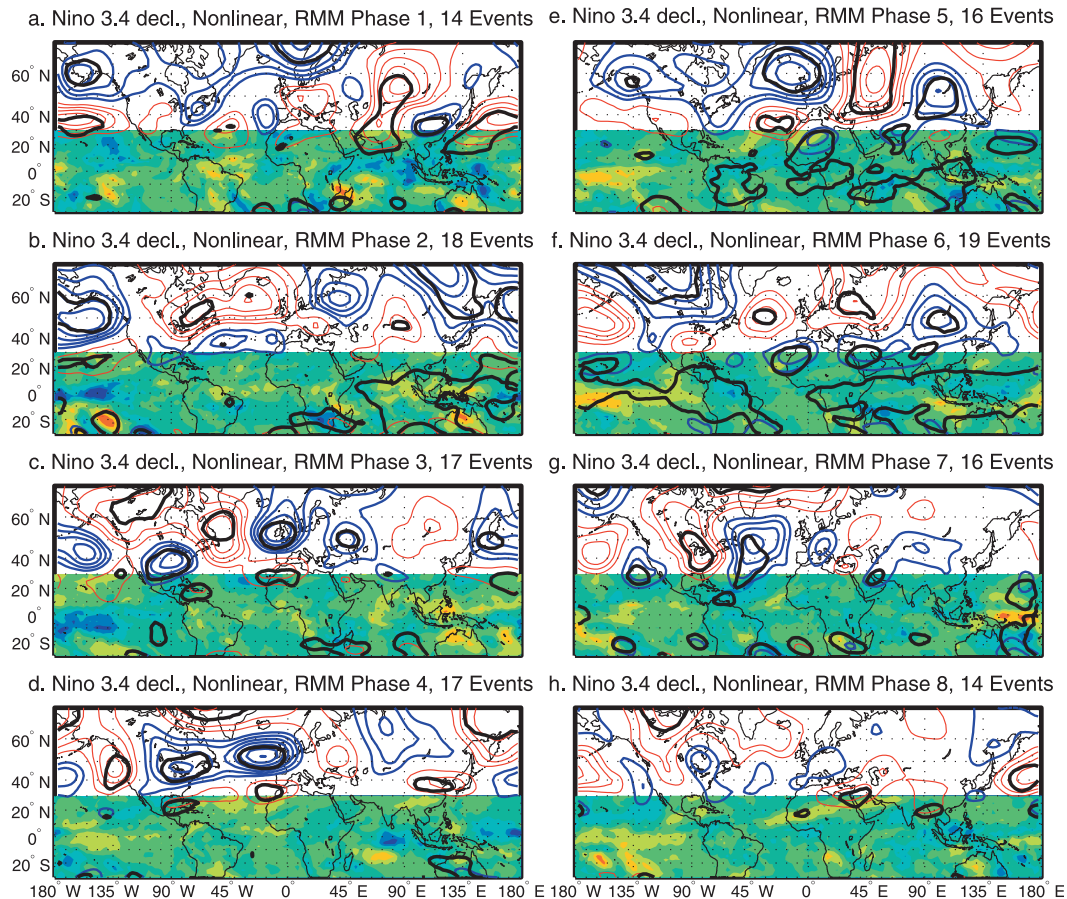
FIG. 6. As in Fig. 5, but for during negative temporal trends in Niño-3.4 SST.

Substantial significant trough anomalies occur in the individual composite for the MJO over Alaska and western Europe during phase 4, and this pattern is significantly more pronounced during cold ENSO. A ridge anomaly that occurs across far northeastern Asia is largely absent when ENSO is not considered. A ridge anomaly over eastern North America is significantly amplified and shifted northward during La Niña.

During phase 5 and cold ENSO, a ridge over the North Atlantic extends farther to the north and east than when the MJO is considered alone. A significant trough anomaly occurs over East Asia that is not present when the MJO is considered by itself, and a trough anomaly over Alaska is substantially amplified. A ridge at the West Coast of the United States present in the individual composite for the MJO is amplified and displaced westward during cold ENSO.

Phase 6 during cold ENSO is statistically similar to phase 6 in the individual composite for the MJO, except that some subtropical trough anomalies are significantly amplified during La Niña, ridge anomalies are enhanced over Europe, and trough anomalies over East Asia are amplified and extend northward.

During MJO phase 7, a trough–ridge–trough pattern extends eastward from eastern North America to the Mediterranean Sea and the subtropical North Atlantic. The central Atlantic ridge and the eastern trough occur with significantly higher amplitude during La Niña.

The simultaneous cold ENSO composite for MJO phase 8 is statistically similar to the individual composite for the MJO, except that convection is more enhanced over the tropical Atlantic.

Figure 5 shows the result of subtracting Figs. 2 and 3b from Fig. 4 to estimate the nonlinear portion of the global OLR and height anomaly pattern associated with MJO activity during La Niña. Solid black contours enclose regions in which the result is significantly different from zero by the bootstrap test discussed in section 2 (these contours are reproduced, for reference, on Fig. 4). Phases 1–7 include substantial anomalies that are significantly different from zero; however, excluding phase 8, significant anomalies attain the smallest geographical extent

a. Nino 3.4 rising, Nonlinear, RMM Phase 1, 17 Events   e. Nino 3.4 rising, Nonlinear, RMM Phase 5, 15 Events

b. Nino 3.4 rising, Nonlinear, RMM Phase 2, 16 Events   f. Nino 3.4 rising, Nonlinear, RMM Phase 6, 14 Events

c. Nino 3.4 rising, Nonlinear, RMM Phase 3, 17 Events   g. Nino 3.4 rising, Nonlinear, RMM Phase 7, 15 Events

d. Nino 3.4 rising, Nonlinear, RMM Phase 4, 23 Events   h. Nino 3.4 rising, Nonlinear, RMM Phase 8, 16 Events

FIG. 7. As in Figs. 5 and 6, but for during positive temporal trends in Niño-3.4 SST.

during phase 1. In general, these residual anomalies appear to favor the North Pacific–North Atlantic regions.

d. Simultaneous composites: Declining ENSO and the MJO

Figure 6 shows the nonlinear portion of the composite resulting from the simultaneous action of each phase of the MJO and declining Niño-3.4 SST, comparable to Fig. 5 for cold ENSO. Results should be considered in comparison with Figs. 2 and 3a, because Fig. 5 gives only the portion of the composite patterns that is not explained by the linear sum of Figs. 2 and 3a.

Results indicate that for phase 1, trough anomalies occur over Alaska and Scandinavia, with enhanced ridge anomalies over central Asia and the temperate latitudes of the North Pacific. During phase 2, enhanced trough anomalies occur over the Gulf of Alaska and East Asia, with enhanced ridge anomalies over eastern Canada. During phase 3, enhanced ridge anomalies occur over northern Canada with enhanced trough anomalies over the eastern United States and western Europe. During phase 4, enhanced ridge anomalies occur off the West Coast of the United States, northeast Asia, and Greenland and trough anomalies over eastern North America, the temperate North Atlantic, and western Europe. Phase 5 is associated with enhanced trough anomalies over the North Atlantic extending across north-central Europe, and across parts of eastern Asia, with substantial significant ridge anomalies over western Russia. Phase 6 is associated with enhanced trough anomalies over far northwestern North America and parts of East Asia, with significant ridge anomalies over the North Atlantic and parts of interior Europe. Phase 7 has enhanced ridge anomalies across eastern North America and Greenland, with enhanced trough anomalies over portions of the western North Atlantic. Phase 8 has enhanced ridge anomalies over northwestern Canada and parts of the western North Pacific.

e. Simultaneous composites: Advancing ENSO and the MJO

The nonlinear portion of composite patterns associated with the MJO during advancing ENSO conditions is shown
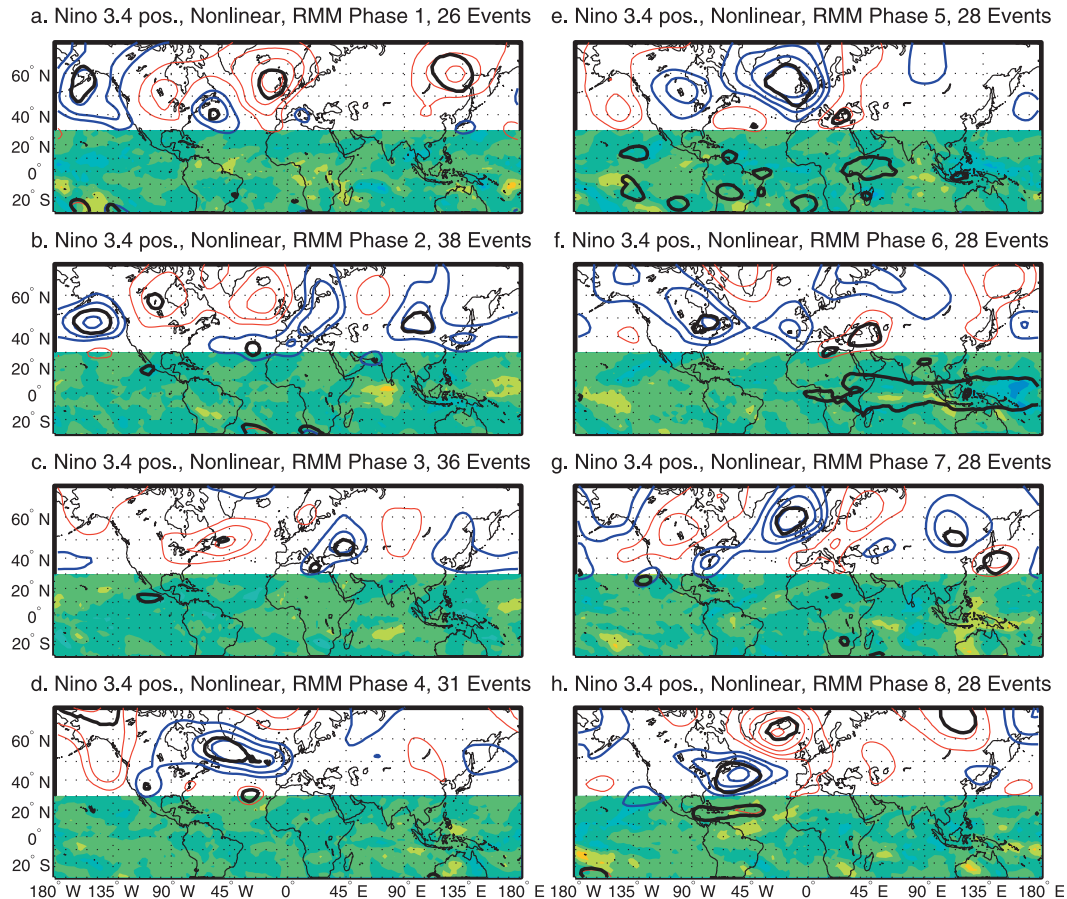
FIG. 8. As in Figs. 5–7, but for warm ENSO (Niño-3.4 SST anomaly >0.5 SDs).

in Fig. 7 (comparable with Figs. 5 and 6 for cold and declining ENSO). During phase 1, enhanced trough anomalies occur over western Russia with enhanced ridge anomalies over East Asia. During phase 2, enhanced ridge anomalies occur over far eastern Asia. A ridge anomaly over the Bering Sea is displaced southward, and a ridge anomaly over Scandinavia is amplified during phase 3. Amplified ridging over central Canada and the northwestern United States occurs during phase 4. During phase 5, enhanced ridge anomalies occur over parts of the eastern North Pacific and Siberia, with enhanced trough anomalies over the southwestern United States, northeastern Asia, and over the Davis Strait and Baffin Bay.

During phase 6 and advancing ENSO, ridge anomalies over the Bering Sea, eastern Europe, and central Asia are substantially enhanced over the individual composite for the MJO. The most substantial significant adjustment to the response to MJO phase 7 during advancing ENSO is enhancement of a trough anomaly over northern Canada. During phase 8, significant enhancement of trough anomalies occurs over northern European

Russia, with enhanced ridge anomalies over portions of East Asia.

f. Simultaneous composites: Warm ENSO and the MJO

The nonlinear part of composite patterns during El Niño conditions is plotted in Fig. 8. Comparison with Fig. 5 shows that in many cases, the global anomaly pattern associated with the MJO during El Niño is roughly the reverse of the signal during La Niña over many regions of the world. However, large anomalies occur in some parts of the world during one phase of the MJO that have no opposite counterpart during the alternate phase of ENSO and the same phase of the MJO. For example, during phase 2 and El Niño, a near-zero height anomaly occurs over the western United States along with a strong negative NAO-like pattern. In contrast, during phase 2 and La Niña, a 50-m trough anomaly is present over the western United States, without a clear expression of an NAO pattern.

g. Geographical and temporal magnitudes of composite patterns

To assess the amplitude of the nonlinear component relative to the amplitude of global anomalies associated with the MJO alone, thick colored lines in Figs. 9a–d show global averages of the absolute values of the nonlinear portion of the composites for declining, cold, increasing, and warm ENSO conditions for each phase of the MJO (horizontal axis). Thin lines of the same colors represent the 95% confidence intervals for the sampling distributions of the means determined from the bootstrap test discussed in section 2. Thick black and the associated thin black curves outline the 95% confidence intervals for the mean absolute anomaly for the individual composites for the MJO. This confidence interval accounts for the number of events included in the simultaneous composites. All curves are approximately flat with respect to the MJO phase (i.e., each MJO phase has roughly the same mean anomaly amplitude within a given composite), except that a local maximum in the nonlinear component is possible near phase 6 during negative and rising ENSO. These results demonstrate that the nonlinear component of the global pattern associated with simultaneous action of the MJO and ENSO is of the same order of magnitude as and in some cases significantly larger than the anomalies associated with the individual composite for the MJO, for each MJO phase. Further, these results suggest that global geopotential height anomalies associated with the MJO might attain higher amplitudes during La Niña than during El Niño, and that the temporal trend of ENSO contributes substantially to these results in comparison with contributions from the absolute state of Niño-3.4 SST.

Although the global mean amplitudes of geopotential height anomalies associated with the MJO do not appear to vary dramatically with the MJO phase, the nonlinear component of the global flow associated with the MJO and ENSO might be more substantial in some geographical regions than others. Figures 10a–d show the absolute values of the composite geopotential height anomalies averaged over all the MJO phases during declining, cold, warming, and warm ENSO, respectively. During each ENSO phase, except Niño-3.4 rising, the largest anomalies associated with the MJO occur over the North Atlantic and regions to the immediate east and west. During Niño-3.4 increasing trends, the strongest composite anomalies occur over the Bering Sea.

h. Contingency analysis of the CPC NAO Index

The structure of the anomalies in Fig. 2 suggests that the global response to the MJO projects onto the loading patterns of the NAO, consistent with the previous results of Cassou (2008) and Lin et al. (2009). The frequent
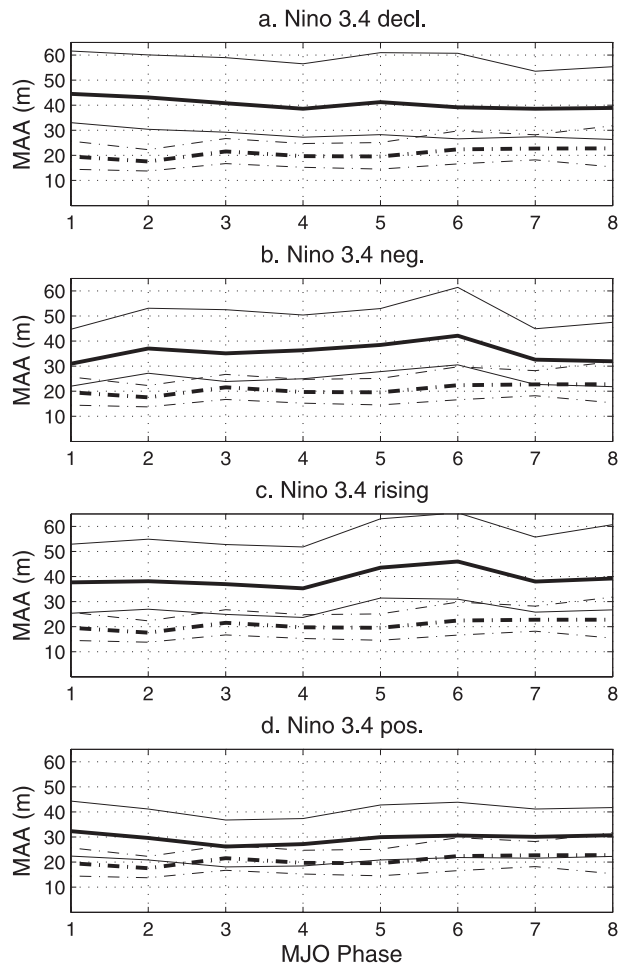
FIG. 9. (a) Absolute values of composite 300-hPa geopotential height anomalies during cooling ENSO averaged over the globe and plotted with respect to the phase of the MJO (thick black curve). (b)–(d) As in (a), except for cold, warming, and warm ENSO, respectively. For reference, the thin solid and thin dashed curves represent the 95% confidence intervals for the thick solid and dashed curves, respectively.

appearance of large anomalies across the North Atlantic in Figs. 4–8 suggests that modulation by ENSO might allow the MJO to explain even greater portions of the signal in the NAO than those previous works have suggested. Cassou (2008) analyzed the anomalous likelihood of achieving either sign of the NAO following each phase of the MJO during October–April. Figure 3 of Cassou (2008) shows his results in a simple contingency diagram of the anomalous probability that the NAO index was of one sign or the other during each Wheeler and Hendon (2004) RMM phase.

To assess the relevance of our findings to the relationship between the MJO and weather over the North Atlantic and Europe, we reproduce the contingency table of Cassou (2008) in our Figs. 11 and 12. The solid gray

a. Nino 3.4 decl.
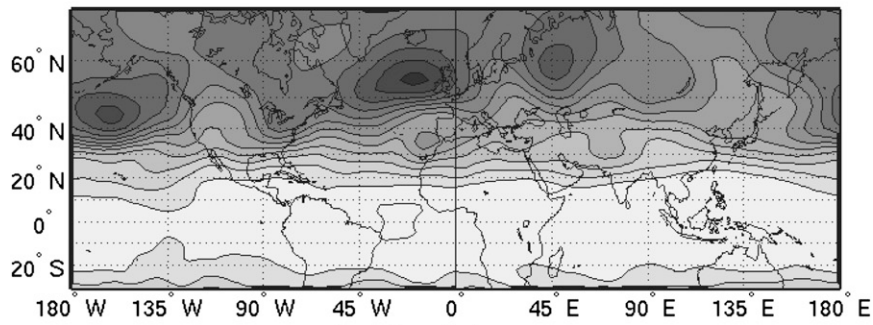
b. Nino 3.4 neg.
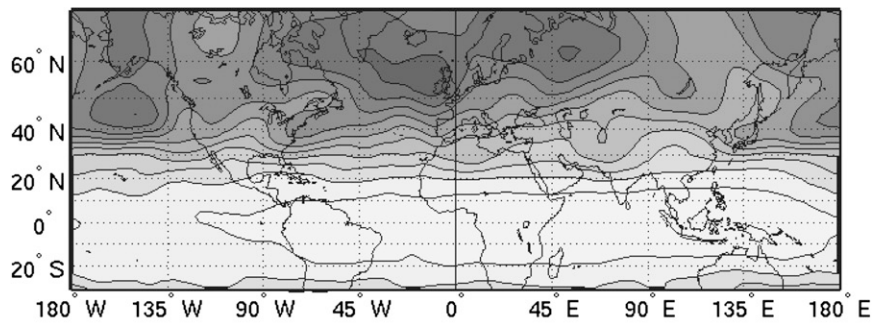
c. Nino 3.4 rising
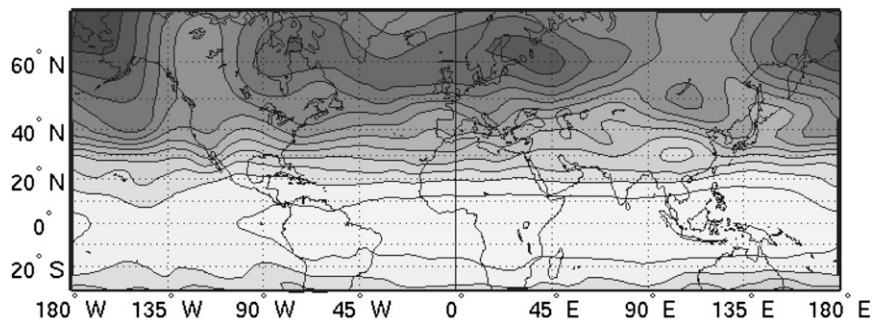
d. Nino 3.4 pos.
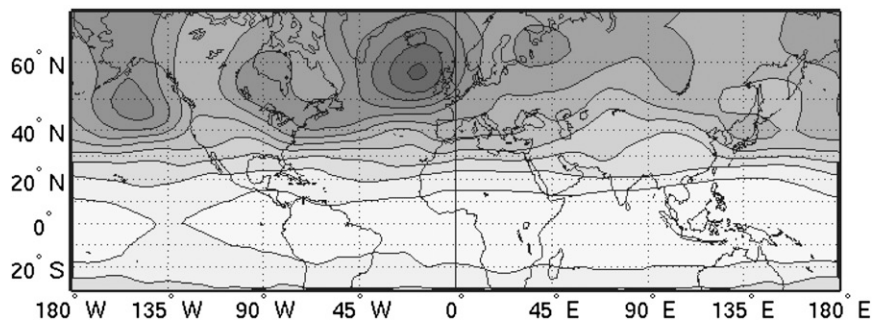
FIG. 10. Absolute values of composite 300-hPa geopotential height anomalies averaged over each phase of the MJO for (a) cooling, (b) cold, (c) warming, and (d) warm ENSO. The contour interval is 5 m, and maximum values exceed 50 m.
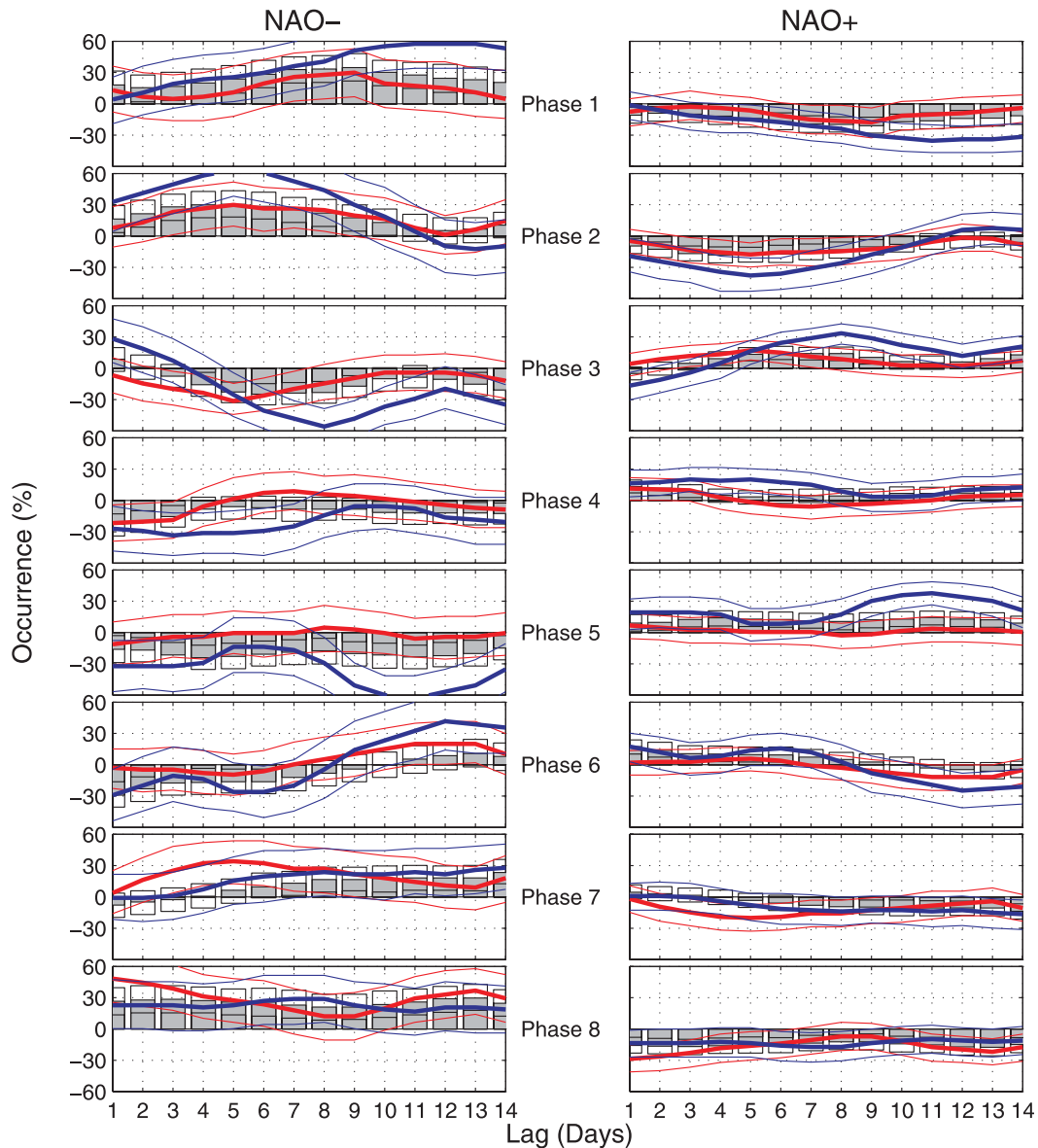
FIG. 11. Contingency diagrams for NAO+ and NAO− and each phase of the MJO, comparable to those of Cassou (2008). Filled bars represent the anomalous fractional occurrence of the event (NAO+ or NAO−) during the listed phases of the MJO. Unfilled bars give the 95% confidence interval for the same probabilities, by a bootstrap test. Thick blue and red curves represent the outcomes, including MJO events during La Niña and El Niño, respectively. Thin red and blue curves give the corresponding 95% confidence intervals. As in Cassou (2008), a zero probability means that the MJO index (or the MJO index during a given phase of ENSO) provides no useful information with respect to the sign of the NAO. A 100% value means that the event is twice as likely during the corresponding MJO phase than otherwise for the climatology during the same season. A −100% value implies that the MJO phase is associated with removal of the background climatological signal.

bars in both Figs. 11 and 12 represent the anomalous fractional probability

$$P = \frac{P_{MJO} - P_{clim}}{P_{clim}}, \qquad (1)$$

where P_{MJO} is the probability that the NAO is a particular sign during a given phase of the MJO and P_{clim} is

the probability that the NAO is of the same sign calculated over the full seasonal climatology. The unshaded bars above and the black horizontal lines below outline the 95% bootstrap confidence interval of P. Our analysis is limited to November–March, for consistency with the remainder of our results. Despite the difference in seasonal focus, the results of Cassou (2008) lie largely within the
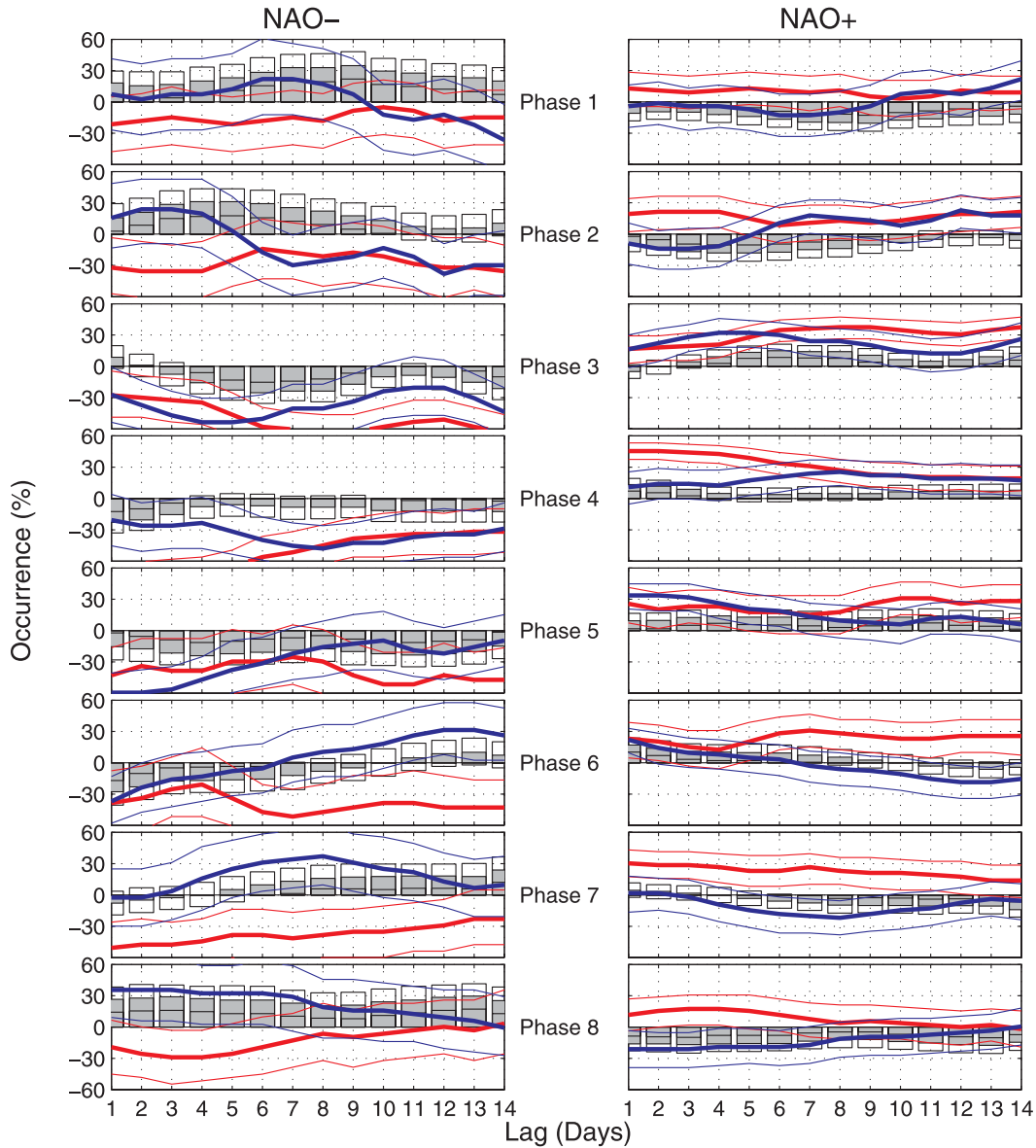
FIG. 12. Contingency diagrams for the NAO index and MJO phase, as in Fig. 11, except that red (blue) curves represent results for increasing (decreasing) trends in the Niño-3.4 SST anomaly.

95% confidence interval for *P* in Figs. 11 and 12. In addition to the bars, we plot curves on Fig. 11 that represent the anomalous probabilities for the sign of the NAO calculated for MJO events during El Niño (thick red curve) and during La Niña (thick blue curve). The thin curves of the same colors outline the corresponding bootstrap 95% confidence intervals. These results demonstrate that La Niña conditions are associated with a dramatically amplified relationship between the MJO and the NAO, whereas results during El Niño are frequently within the range for the MJO without considering ENSO. The NAO index seems to respond most strongly during La Niña conditions

following phases 1, 5, and 6, although the normal temporal evolution of the MJO causes patterns observed during one phase to occur roughly between a lag of 5 and 8 days later than the timing of similar patterns during the subsequent phase. To illustrate, the blue curve associated with the NAO during La Niña bends upward near lag +14 days. That region of upward slope is roughly consistent with the blue curve near lag +6 to +7 days following phase 6. The maximum achieved following phase 6 near lag +12 days also appears near lag +6 to +7 days during phase 7.

   The thick red and blue curves in Fig. 12 represent the corresponding contingency diagrams for increasing or

decreasing Niño-3.4 SST (respectively), with thin curves of the same colors outlining the corresponding 95% confidence intervals. Figures 12a and 12b, taken together, suggest that warming ENSO is associated with increased likelihood for NAO+ and decreased likelihood for NAO−. After accounting for the background bias in the results for warming ENSO (not shown), the probability of occurrence of NAO+ or NAO− frequently appears to move in opposite directions in time after the same MJO phase but opposite trends in ENSO.

5. Conclusions

A simple composite analysis demonstrates the global patterns associated with the simultaneous action of the MJO and ENSO during the Northern Hemisphere cold season. Substantial anomalies around the globe associated with such simultaneous action are not explained by simple linear combinations of composites based on the MJO and ENSO separately. These results demonstrate that when both modes are present at the same time, both need to be considered simultaneously to diagnose the associated global weather patterns. Results suggest that the global mean absolute amplitude of anomalies associated with nonlinear behavior is relatively evenly distributed across the MJO phase. Variance in 300-hPa geopotential height anomalies associated with this nonlinear behavior is strongly concentrated over the North Atlantic and the Bering Sea regions. Although the linear response to El Niño and La Niña over Europe is small, our results suggest that ENSO might substantially influence the weather over Europe by amplifying and modulating the sign of the extratropical response to the MJO over the North Atlantic. Results confirm the work of Cassou (2008) and Lin et al. (2009) that the North Atlantic Oscillation indexes vary strongly with the MJO. We further demonstrate that the association of the MJO with the CPC index of the NAO is substantially stronger during cold ENSO conditions, and that the temporal trend of ENSO also combines with the MJO to strongly influence this index.

Our results demonstrate that the global response to the MJO changes with ENSO. Others have demonstrated that extratropical patterns influence the large-scale organization of moist deep convection in the tropics (e.g., Hoskins and Yang 2000; Kiladis et al. 2009). It follows that the modulation of extratropical patterns associated with the MJO might somehow modify the propagation and structure of the MJO itself.

The authors are presently analyzing the effects of the modulation of the global response to the MJO by ENSO on more specific global weather patterns, such as severe weather over the United States, behaviors of cutoff,

upper-level lows over eastern North America, and tropical cyclogenesis. Recently, Roundy and Schreck (2009) introduced a two-dimensional phase diagram for tracking the progress of tropical convective anomalies associated with ENSO. One potential area of further work is to reproduce and extend this analysis by compositing MJO events during specific phases of ENSO diagnosed from this phase space.

REFERENCES

Bladé, I., and D. L. Hartmann, 1995: The linear and nonlinear extratropical response to tropical intraseasonal heating. *J. Atmos. Sci.,* **52,** 4448–4471.

Brankovic, C., T. Palmer, and L. Ferranti, 1994: Predictability of seasonal atmospheric variations. *J. Climate,* **7,** 217–237.

Branstator, G. W., 2002: Circumglobal teleconnections, the jet stream waveguide, and the North Atlantic Oscillation. *J. Climate,* **15,** 1893–1910.

Cassou, C., 2008: Intraseasonal interaction between the Madden-Julian Oscillation and the North Atlantic Oscillation. *Nature,* **455,** 523–527.

Charney, J. G., and J. Shukla, 1981: Predictability of monsoons. *Monsoon Dynamics,* J. Lighthill and R. Pearce, Eds., Cambridge University Press, 99–130.

Ferranti, L., T. N. Palmer, F. Molteni, and K. Klinker, 1990: Tropical–extratropical interaction associated with the 30-60 day oscillation and its impact on medium and extended range prediction. *J. Atmos. Sci.,* **47,** 2177–2199.

Hendon, H. H., B. Liebmann, M. Newman, J. D. Glick, and J. E. Schemm, 2000: Medium-range forecast errors associated with active episodes of the Madden–Julian oscillation. *Mon. Wea. Rev.,* **128,** 69–86.

Higgins, R. W., J.-K. E. Schemm, W. Shi, and A. Leetmaa, 2000: Extreme precipitation events in the western United States related to tropical forcing. *J. Climate,* **13,** 793–820.

Hoskins, B. J., and G.-Y. Yang, 2000: The equatorial response to higher latitude forcing. *J. Atmos. Sci.,* **57,** 1197–1213.

Jin, F., and B. J. Hoskins, 1995: The direct response to tropical heating in a baroclinic atmosphere. *J. Atmos. Sci.,* **52,** 307–319.

Jones, C., and J.-K. E. Schemm, 2000: The influence of intraseasonal variations on medium-range weather forecasts over South America. *Mon. Wea. Rev.,* **128,** 486–494.

——, D. E. Waliser, K. M. Lau, and W. Stern, 2004a: Global occurrences of extreme precipitation and the Madden–Julian oscillation: Observations and predictability. *J. Climate,* **17,** 4575–4589.

——, ——, ——, and ——, 2004b: The Madden–Julian oscillation and its impact on Northern Hemisphere weather predictability. *Mon. Wea. Rev.,* **132,** 1462–1471.

Kalnay, E., and Coauthors, 1996: The NCEP/NCAR 40-Year Reanalysis Project. *Bull. Amer. Meteor. Soc.,* **77,** 437–471.

Kiladis, G. N., M. C. Wheeler, P. T. Haertel, K. H. Straub, and P. E. Roundy, 2009: Convectively coupled equatorial waves. *Rev. Geophys.,* **47,** RG2003, doi:10.1029/2008RG000266.

Liebmann, B., and C. A. Smith, 1996: Description of a complete (interpolated) outgoing longwave radiation dataset. *Bull. Amer. Meteor. Soc.,* **77,** 1275–1277.

Lin, H., G. Brunet, and J. Derome, 2009: An observed connection between the North Atlantic Oscillation and the Madden–Julian oscillation. *J. Climate,* **22,** 364–380.

Matthews, A. J., B. J. Hoskins, and M. Masutani, 2004: The global response to tropical heating in the Madden-Julian oscillation during northern winter. *Quart. J. Roy. Meteor. Soc.,* **130,** 1991–2011.

Mo, K. C., 2000: Intraseasonal modulation of summer precipitation over North America. *Mon. Wea. Rev.,* **128,** 1490–1505.

——, and R. W. Higgins, 1998: Tropical influences on California precipitation. *J. Climate,* **11,** 412–430.

Nogues-Paegle, J., L. A. Byerle, and K. C. Mo, 2000: Intraseasonal modulation of South American summer precipitation. *Mon. Wea. Rev.,* **128,** 837–850.

Pohl, B., and A. J. Matthews, 2007: Observed changes in the lifetime and amplitude of the Madden–Julian oscillation associated with interannual ENSO sea surface temperature anomalies. *J. Climate,* **20,** 2659–2674.

Roundy, P. E., 2008: Analysis of convectively coupled Kelvin waves in the Indian Ocean MJO. *J. Atmos. Sci.,* **65,** 1342–1359.

——, and W. M. Frank, 2004: A climatology of waves in the equatorial region. *J. Atmos. Sci.,* **61,** 2105–2132.

——, and J. R. Kravitz, 2009: The association of the evolution of intraseasonal oscillations with ENSO phase. *J. Climate,* **22,** 381–395.

——, and C. Schreck, 2009: A combined wave-number–frequency and time-extended EOF approach for tracking the progress of modes of large-scale organized tropical convection. *Quart. J. Roy. Meteor. Soc.,* **135,** 161–173.

——, C. J. Schreck, and M. A. Janiga, 2009: Contributions of convectively coupled equatorial Rossby waves and Kelvin waves to the real-time multivariate MJO indices. *Mon. Wea. Rev.,* **137,** 469–478.

Sardeshmukh, P. D., and B. J. Hoskins, 1988: The generation of global rotational flow by steady idealized tropical divergence. *J. Atmos. Sci.,* **45,** 1228–1251.

Wallace, J. M., and D. S. Gutzler, 1981: Teleconnections in the geopotential height field during Northern Hemisphere winter. *Mon. Wea. Rev.,* **109,** 784–812.

Weickmann, K. M., and P. D. Sardeshmukh, 1994: The atmospheric angular momentum cycle associated with a Madden–Julian oscillation. *J. Atmos. Sci.,* **51,** 3194–3208.

——, and E. Berry, 2007: A synoptic–dynamic model of subseasonal atmospheric variability. *Mon. Wea. Rev.,* **135,** 449–474.

——, and ——, 2009: The tropical Madden–Julian oscillation and the global wind oscillation. *Mon. Wea. Rev.,* **137,** 1601–1614.

——, G. N. Kiladis, and P. D. Sardeshmukh, 1997: The dynamics of intraseasonal atmospheric angular momentum oscillations. *J. Atmos. Sci.,* **54,** 1445–1461.

Wheeler, M., and G. N. Kiladis, 1999: Convectively coupled equatorial waves: Analysis of clouds and temperature in the wavenumber–frequency domain. *J. Atmos. Sci.,* **56,** 374–399.

——, and H. H. Hendon, 2004: An all-season real-time multivariate MJO index: Development of an index for monitoring and prediction. *Mon. Wea. Rev.,* **132,** 1917–1932.

Wilks, D. S., 2006: *Statistical Methods in the Atmospheric Sciences.* Academic Press, 627 pp.

Zhang, C., 2005: Madden-Julian Oscillation. *Rev. Geophys.,* **43,** RG2003, doi:10.1029/2004RG000158.